Constant-Frequency and Noncommunication-Based Inductive Power Transfer Converter for Battery Charging

Io-Wa Iam , *Student Member, IEEE*, Iok-U Hoi, *Student Member, IEEE*, Zhicong Huang , *Member, IEEE*,
Cheng Gong , *Graduate Student Member, IEEE*, Chi-Seng Lam , *Senior Member, IEEE*,
Pui-In Mak , *Fellow, IEEE*, and Rui Paulo Da Silva Martins , *Fellow, IEEE*

Abstract—Compared with conductive charging, wireless inductive-power-transfer (IPT) charging exhibits higher potential as it avoids physical contact and provides convenient user experience. Regrettably, it is challenging for IPT converters to comply with the constant current (CC) and constant voltage (CV) charging profiles, while optimizing power efficiency. To achieve such goals, the existing IPT converters can apply multistage converter, dual side, or variable frequency modulation with feedback wireless communication. However, applying multistage converter increases cost and loss, while the stability of the IPT converter with dual side or variable frequency modulation can be at risk if communication fails. This article proposes a single-stage IPT converter for battery charging. With a constant operating frequency and without feedback wireless communication, the receiver side directly regulates the output to comply with the CC/CV charging profile, while the transmitter side aids in the reduction of the modulated phase shift angle at the receiver side, thus improving the efficiency. No wireless communication between the transmitter and receiver sides benefits both the hardware cost and stability. Also, we implement implicitly an output voltage regulation, further avoiding the need of an extra dc–dc converter. We verify experimentally the proposed control method in a 1-KW charging platform with a measured peak efficiency up to 94.35%.

Index Terms—Constant current (CC) charging, constant operating frequency, constant voltage (CV) charging, no wireless communication, wireless inductive-power-transfer (IPT) charging.

I. INTRODUCTION

WITH fast growing of electronics device market, different ways of charging have attracted more and more attention. With benefits of safety and convenience, wireless charging occupies a great significant position in the electronics device market, such as mobile devices and autoguided vehicles [1]–[4]. Nowadays, inductive power transfer (IPT) system has been commonly used for wireless battery charging, which transfers power via magnetic coupling between the transmitter side and the receiver side [5]. Compared with traditional conductive charger, an IPT system can deliver power over an air gap instead of using plugs and cables, avoiding unsafe issues of electric damage and shock [6], [7]. In general, lithium-ion battery is widely used in most of the electronics applications. Its typical charging profile mainly includes a constant-current (CC) charging stage and a constant voltage (CV) charging stage, as shown in Fig. 1. Since the charging current at the completion of the CV charging stage is as low as 10% of its rated value, the equivalent load range of the battery is very wide, making a challenge to the IPT converter in providing a stable and efficient battery charging process.

To comply with the battery charging profile, it is an intuitive idea to add an extra dc–dc converter to the output terminal of the IPT converter for power regulation [8]–[11]. Obviously, extra losses and cost from additional power stage are inevitable such that the efficiency of the IPT system will be degraded. To avoid the extra power losses of the additional converter stage, a single-stage IPT converter can utilize its native load-independent current (LIC) and load-independent voltage (LIV) transfer characteristics for CC charging and CV charging, respectively. In some studies [12], [13], the single-stage IPT converter includes hybrid compensation topologies and some active switches for the transition from the LIC mode to the LIV mode. For example, the IPT converter in [12] includes a series–series (SS) compensation circuit and a parallel–series

TABLE I

COMPARISON AMONG PREVIOUS WORKS AND THIS WORK FOR ACHIEVING IPT CHARGING

|			Type of IPT Compensation	Extra DC-DC Converter	Frequency Control	Wireless Communication	Soft Switching
Multi-stage		[8]-[11]	SS	Yes	No	Yes	No
Load-independent transfer characteristic	Hybrid-topology	[12],[13]	Hybrid SS-PS/SP-PP	No	No	Yes	No
	Frequency-hopping	[14],[15]	SS, LCC-LCC	No	Yes	Yes	Yes
Dual-side phase-shift PWM		[18]-[20]	SS	No	No	Yes	No
Coordinate frequency and conduction angle		[21]	SS	No	Yes	Yes	Yes
This work			SS	No	No	No	Yes
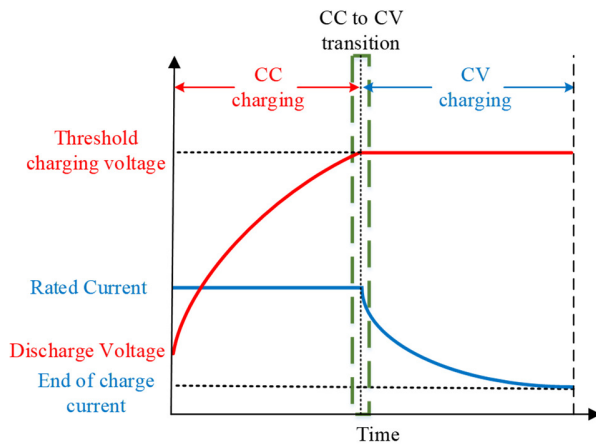
Fig. 1. Typical charging profile of lithium-ion battery, CC and CV charging.

compensation circuit for the CC charging and the CV charging, respectively. The drawback of such hybrid-compensation scheme is that the two sets of compensations circuits and the additional power switches increase the cost. To eliminate the extra power switches and the sparing compensation circuits, a single-stage IPT converter can operate at different operating frequencies for the LIC mode and the LIV mode [14], [15]. By hopping the operating frequency, CC charging and CV charging can be achieved without using hybrid compensation circuits. Nevertheless, efficiency optimization is not considered in both hybrid-compensation and frequency-hopping schemes, because the circuit cannot provide load matching ability [16], [17]. It is reported in [18] and [19] that the IPT converter with dual-sided active switches can provide output regulation as well as load matching for efficiency enhancement for a wide load range, but they suffer from hard switching, thus increasing the whole converter power loss. A novel dual-sided phase shift pulsewidth modulation (PWM) control is presented in [20], which achieves soft switching and improves the output performances, but it requires additional auxiliary branch circuits on the receive side, thus increasing the cost. In [21], a single-stage IPT converter can achieve power regulation, efficiency optimization and soft switching, by coordinately modulating the operating frequency in the primary side and the conduction angle in the secondary side. However, since frequency modulation is implemented in the primary side,

wireless feedback communication is needed, which is risky if the communication fails.

To address the drawbacks of the aforementioned IPT schemes [8]–[21] for battery charging, this article proposes a control strategy with constant-frequency and noncommunication-based single-stage IPT converter for battery charging as shown in Fig. 2. The semiactive rectifier (SAR) at the receiver side modulates the load impedance for direct power regulation, while the full-bridge inverter at the transmitter side operates at a constant switching frequency with phase shift PWM for efficiency optimization. The proposed control strategy enables stable CC and CV charging for the battery, and it has the following contributions and benefits.

1) A constant operation frequency for the whole charging profile simplifies the hardware design (Section IV).
2) No feedback wireless communication lowers the risk of instability during charging (Section IV).
3) Improved charging efficiency over a wide load range (Section V).
4) Fully soft switching is achieved at both the inverter and SAR of the SSIPT converter under simple control (Section V).
5) Immune to misalignment to achieve constant output voltage and current, while upholding a high efficiency (Section V).
6) Direct power regulation is provided at the receive side (Section IV).
7) No extra dc–dc converter saves the hardware cost (Section I).

The comparison of the achievable features between our proposed scheme and the schemes in literature are summarized in Table I. Table II also shows the comparison of number of components among previous works and our proposed work.

The rest of this article is organized as follows. Section II describes the IPT system structure and the proposed control modulation techniques for battery charging. And charging efficiency and soft switching via the equivalent circuit model will be analyzed and discussed in Section III. In Section IV, the implementation and stability study of the proposed control scheme for the whole charging profile is presented, and the experimental verification of output waveforms and charging performance is given in Section V. Finally, Section VI concludes this article.
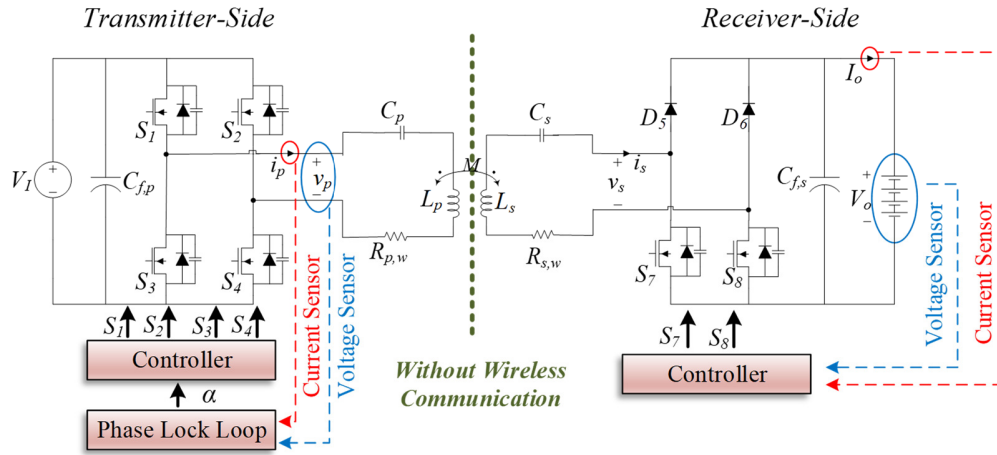
Fig. 2. Circuit configuration of SSIPT converter and its control scheme.

TABLE II
COMPARISON OF NUMBER OF COMPONENTS AMONG PREVIOUS WORKS AND THIS WORK

			No. Switches	Extra DC-DC Converter	No. Sensors	Wireless Communication Components
Multi-Stage		[8]	8	1	3	Yes
		[9]	6	1	3	Yes
		[10]	6	1	3	Yes
		[11]	7	2	1	Yes
Load-independent transfer characteristic	Hybrid-topology	[12]	7	No	2	Yes
		[13]	6	No	1	Yes
	Frequency-hopping	[14]	4	No	2	Yes
		[15]	4	No	2	Yes
Dual-side phase-shift PWM		[18]	6	No	3	Yes
		[19]	8	No	4	Yes
		[20]	10	No	NA	NA
Coordinate frequency and conduction		[21]	6	No	NA	Yes
This work			6	No	4	No

II. IPT SYSTEM STRUCTURE AND PROPOSED CONTROL MODULATION TECHNIQUES

A. SS Compensated IPT Converter

The circuit configuration of the SS IPT converter is shown in Fig. 2, which includes an input voltage source V_I, an input capacitor $C_{f,p}$, a full bridge inverter, a resonant tank with SS compensation, and an SAR with output capacitor $C_{f,s}$, where the subscript "p" and subscript "s" indicate the parameters at the transmitter side or at the receiver side, respectively. At the transmitter side, the full-bridge inverter includes four transistors S_1–S_4, which are controlled by using the phase shift PWM, to invert the dc input voltage V_I into high-frequency ac voltage v_p at the transmitter side. i_p is transmitter side ac current. The loosely coupled transformer has primary self-inductance L_p, secondary self-inductance L_s, and mutual inductance M. For the conventional transformer, the coupling coefficient can be defined as $k = (M/(L_pL_s)^{1/2})$. Both winding coils of the loosely coupled transformer are series compensated by the series compensation capacitors C_p and C_s. The coil losses at the transmitter side and the receiver side are represented by resistors R_p and R_s, respectively. The resonant frequencies of the transmitter side and receiver side are given by

$$\omega_p = \frac{1}{\sqrt{L_pC_p}} \tag{1}$$

$$\omega_s = \frac{1}{\sqrt{L_sC_s}}. \tag{2}$$

At the receiver side, v_s and i_s are the receiver side ac current voltage and current. Then this high frequency ac power is converted into dc power by the SAR, which consists of two transistors S_7 and S_8 at lower part and two passive diodes D_5 and D_6 at upper part. The resonant circuit is a high Q circuit whose electrical characteristic is dominated by the fundamental component of a Fourier series representation of the actual waveform. Since the resonant circuit output voltage and current (v_s and i_s) to the SAR are in phase, it is acceptable to model the load as a pure resistor. Moreover, the charging process is much slower than the resonant period of the SSIPT converter, thus the battery can be modeled as a resistor R_{battery} theoretically, which is determined by the dc
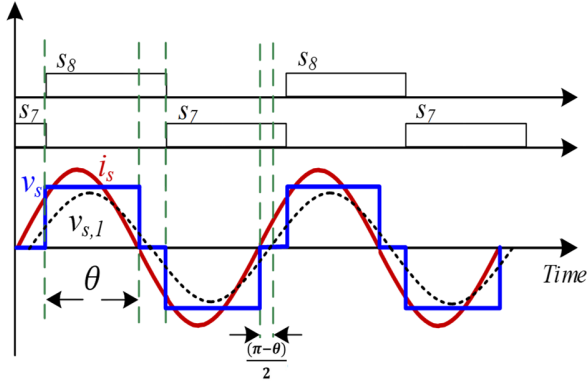
Fig. 3.   Operating waveform of phase shift modulation at receiver-side SAR.

Fig. 4.   Operating waveform of inverter (top) before and (bottom) after applying modulation at transmitter side.

charging voltage V_O and the dc charging current I_O [21]–[23]

$$R_{\text{Battery}} = \frac{V_O}{I_O}. \tag{3}$$

It aims to indicate the amount of power obtained from the charger. However, in the literature [14], [21]–[28], the battery is available to be modeled as a resistor.

B. Control Modulation Techniques of SAR and Inverter

The SAR at the receiver side in Fig. 2 can regulate the output current by varying its conduction angle, thus it does not require an extra dc–dc converter for regulating the output voltage in comparison with those multistage designs [8]–[11]. The phase shift PWM technique is applied for controlling the SAR by controlling S_7 and S_8. S_7 and S_8 are complement to each other and both kept turning on for half of a cycle. S_7 is turned on with a time delay of π -θ to the zero-crossing point where i_s commutating from positive to negative, while S_8 is turned on with a time delay of π -θ to the zero-crossing point where i_s commutating from negative to positive. The switching sequences and operating waveforms are shown in Fig. 3. $v_{s,1}$ is the fundamental component of v_s. From Fig. 3, it can be observed that $v_{s,1}$ lags i_s by a phase angle of $(\pi - \theta)/2$. [29], [30]. Zero voltage switching (ZVS) can be achieved for the MOSFET switches of SAR [18], [31]–[33]. It has been studied in [21] that the SAR as well as the load can be modeled as an equivalent impedance, which can be expressed as

$$Z_{\text{eq}} = R_{\text{eq}} + j X_{\text{eq}} \tag{4}$$

$$R_{\text{eq}} = \frac{8}{\pi^2} R_{\text{Battery}} \sin^4\left(\frac{\theta}{2}\right) \tag{5}$$

$$X_{\text{eq}} = -\frac{8}{\pi^2} R_{\text{Battery}} \sin^3\left(\frac{\theta}{2}\right) \cos\left(\frac{\theta}{2}\right). \tag{6}$$

As shown in (6), as the modulated phase shift angle θ of the SAR decreases, the reactive component of the equivalent load will increase as well, leading to significant efficiency degradation. Therefore, a phase shift PWM proposed in [28], [34], and [35] will be adopted in the transmitter-side inverter part in this article to help for reducing the extent of modulated phase shift angle θ. $v_{p,1}$ is the fundamental component of v_p. The input phase angle β is derived based on considering
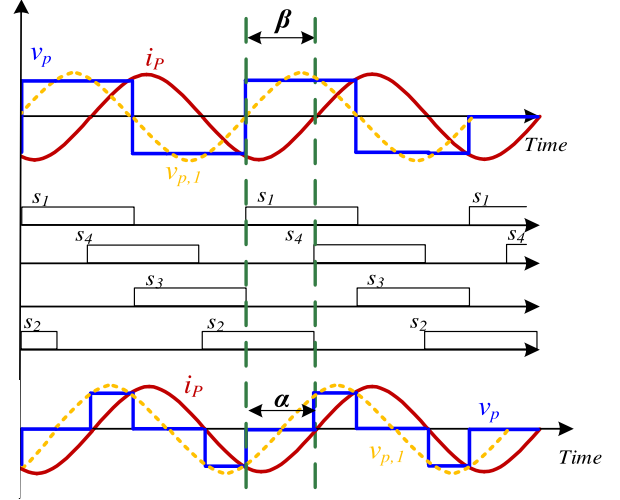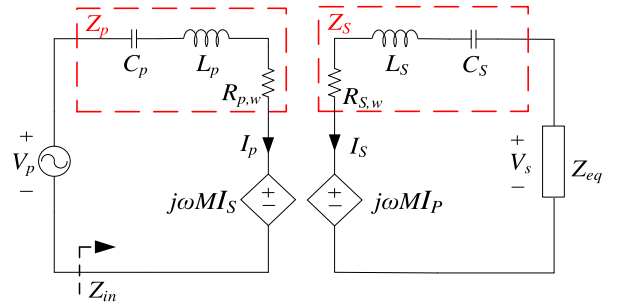

Fig. 5.   Fundamental frequency equivalent circuit.

the fundamental waveforms of v_p and i_p. Before applying the phase shift PWM at the inverter, i_p lags the fundamental waveform of primary voltage $v_{p,1}$ by a phase angle β. The maximum conduction angle of transmitter-side input voltage v_p is defined as α. When the phase shift PWM is applied, the modulation of the inverter is done by changing the conduction angle α according to the input phase angle. For the operation of switches in inverter, S_1 and S_3 are complement to each other. And S_4 is turned on with time delay of α related to S_1, while S_2 is turned on with time delay of α related to S_3, aiming to lead the v_p and i_p to be in phase, as shown in Fig. 4.

III. IPT SYSTEM CIRCUIT MODEL, CHARGING EFFICIENCY AND SOFT-SWITCHING ANALYSIS

A. Equivalent Circuit Model

For steady-state analysis, the SSIPT converter can be simplified by only considering the fundamental components [37]–[39]. Fig. 5 shows the equivalent circuit model of SSIPT converter based on fundamental approximation. The phasors of fundamental components of v_p, i_p, v_s, i_s can be represented as $\boldsymbol{V}_p$, $\boldsymbol{I}_p$, $\boldsymbol{V}_s$, and $\boldsymbol{I}_s$. ω is the operating frequency of converter. For simplicity, the winding resistance of both coils are assumed to be small,

which can be neglected for the following analysis, that is, $R_{p,w} \approx R_{s,w} \approx 0$. From Fig. 5

$$V_p = Z_p I_p - j\omega M I_s \tag{7}$$

$$0 = j\omega M I_p - (Z_s + Z_{eq}) I_s. \tag{8}$$

From (7) and (8), we can get the relationship between i_s and i_p

$$I_s = \frac{j\omega M}{Z_{eq} + Z_s} I_p \tag{9}$$

$$I_p = \frac{V_p}{Z_p + \frac{\omega^2 M^2}{Z_s + Z_{eq}}} \tag{10}$$

where

$$Z_P = j\omega L_P + \frac{1}{j\omega C_P} + R_{P,w}, \quad Z_S = j\omega L_S + \frac{1}{j\omega C_S} + R_{S,w}$$

are the impedance at transmitter side and receiver side, respectively.

B. Charging Efficiency and Soft-Switching

From Fig. 5, the corresponding charging efficiency of the SSIPT converter can be expressed as

$$\eta = \frac{I_s^2 R_{eq}}{I_s^2 R_{eq} + I_s^2 R_{S,w} + I_p^2 R_{p,w}}. \tag{11}$$

Combined with (9)–(11), the charging efficiency can be simplified as (12), as shown at the bottom of the page.

To achieve maximum power efficiency, ω_S is designed at its optimum operating frequency ω_{opt} [8], [40] as

$$\omega_{opt} = \omega_s. \tag{13}$$

And the maximum power efficiency can be achieved as

$$\eta_{opt} \approx \frac{1}{\frac{\sqrt{R_{p,W} R_{s,W}}}{\omega_{opt} M} + 1} \tag{14}$$

if and only if R_{eq} and X_{eq} are fulfilled in their optimum values [21], which are given in the following equation:

$$R_{opt} = \omega_{opt} M \sqrt{\frac{R_{s,w}}{R_{p,w}}} \tag{15}$$

$$X_{eq,opt} = \frac{1}{\omega_{opt} C_s} - \omega_{opt} L_s. \tag{16}$$

In addition, the modulated phase shift angle θ of the SAR also affects the SSIPT converter charging efficiency, as given in Fig. 6. Since decreasing θ will create larger equivalent load reactance, as indicated by (6), charging efficiency drops significantly, and vice versa. The solution for relaxing the effect of the modulated phase shift angle θ will be discussed in Section IV-B.
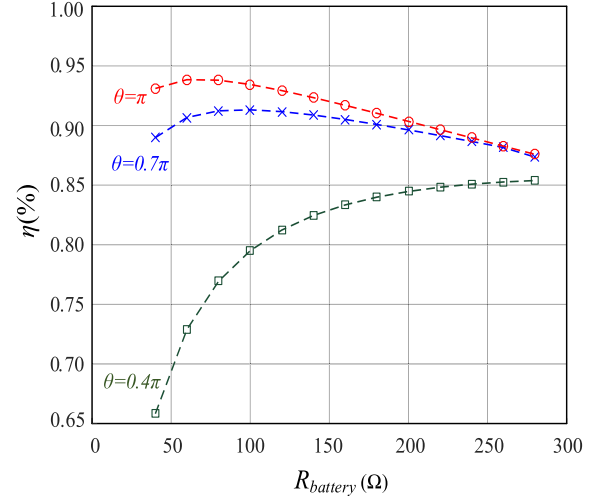
Fig. 6. Simulated charging efficiency versus load resistance $R_{Battery}$ for various phase shift angle θ.
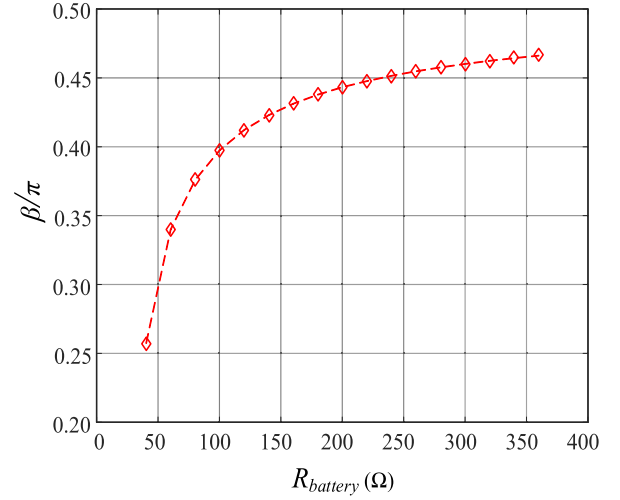
Fig. 7. Input phase angle β versus load resistance $R_{battery}$.

For the considerations of soft switching technique, the input impendence Z_{in} and its corresponding input phase angle β should be analyzed, which are given as

$$Z_{in} = R_{p,w} + Z_p + \frac{(\omega M)^2}{R_{eq} + R_{s,w} + (Z_s + jX_{eq})} \tag{17}$$

$$\beta = \frac{1}{\pi} \arctan \left| \frac{\text{Im}(Z_{in})}{\text{Re}(Z_{in})} \right|. \tag{18}$$

By using the simulation parameters as in Table III, Fig. 7 shows the input phase angle versus load resistance with the phase shift modulation. As the input phase angle is always positive, that means its input impedance keeps inductive, ZVS can be naturally achieved not only at the SAR part, but also at the inverter part.

$$\eta = \frac{(\omega M)^2 R_{eq}}{(\omega M)^2 (R_{eq} + R_{s,w}) + R_{s,w} \left[(R_{eq} + R_{s,w})^2 + \left(X_{eq} + \omega L_s - \frac{1}{\omega C_s} \right)^2 \right]}. \tag{12}$$

IV. IMPLEMENTATION OF CC AND CV CHARGING

A. CC Charging

As the inherent CC output characteristic (also called LIC output characteristic [41]) of the SSIPT converter, during alignment case, the control of SAR and inverter is not necessary for CC charging. Operating in this way, the SSIPT converter can achieve the optimum efficiency at full power. Therefore, the SAR can be operate as a passive rectifier, that is

$$\theta = \pi. \tag{19}$$

While the operating frequency and the conduction angle of the inverter can be approximately fixed at

$$\omega = \omega_p \tag{20}$$
$$\alpha = 0 \tag{21}$$

respectively. During the CC charging period, no matter what the loading is, the phase shift and conduction angles for the SAR and inverter are kept at the same as $\theta = \pi$, $\alpha = 0$. Fig. 8 shows the operating points of loading of $R_{\text{battery}} = 10$ and 20 Ω, which keep $\theta = \pi$, $\alpha = 0$ during CC charging. An approximated CC output can be achieved by neglecting the coil losses and converter losses, given by

$$I_O \approx \frac{8}{\pi^2} \frac{|V_P|}{\omega_P M}. \tag{22}$$

In general, the ratio of (ω_p/ω_s) is set at unity to achieve LIC of the SSIPT converter. To realize ZVS of the MOSFET in the inverter during CC charging, the practical resonant frequency of transmitter side ω_p is usually designed to be slightly smaller than resonant frequency of receiver side ω_s ($\omega_{\text{opt}} = \omega_s$), without changing the operating frequency, which indicates the resonant frequency is slightly smaller than the operating frequency at the transmitter side [41]. Moreover, by locating the optimum efficiency point of the SSIPT converter at full power, that is,

$$R_{\text{opt}} = \frac{V_{\text{rated}}}{I_O}. \tag{23}$$

V_{rated} is the threshold charging voltage of the battery. The maximum efficiency will be designed near the completion of the CC charging stage. Due to the relatively narrow load range during the CC charging process, the efficiency will not deviate from the maximum point too much even at the beginning of the CC charging. Therefore, high efficiency can be maintained for the whole CC charging process.

Indeed, when the misalignment happens, the output current of the SSIPT converter increases accordingly. From Fig. 9, the output current's monitoring and regulation is implemented for the controller at the receiver side. However, under misalignment case, the controller of SAR will work on output current regulation to maintain the dc output current by adjusting the phase shift angle θ at SAR. Moreover, as the operation of SAR, the input phase angle becomes positive and the control of conduction angle α at the inverter will be operated accordingly. The operation of inverter is similar with CV
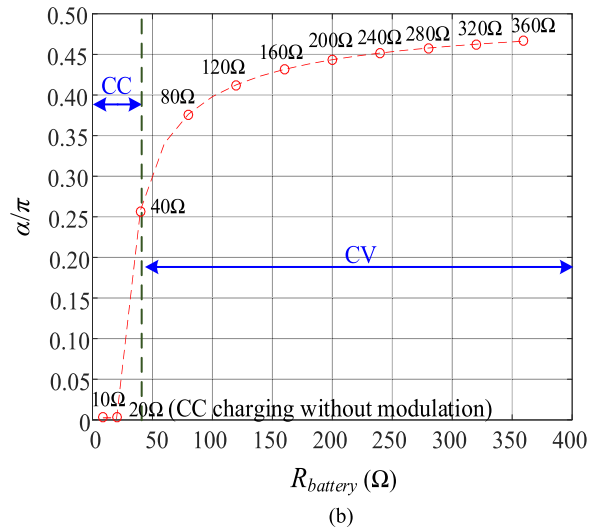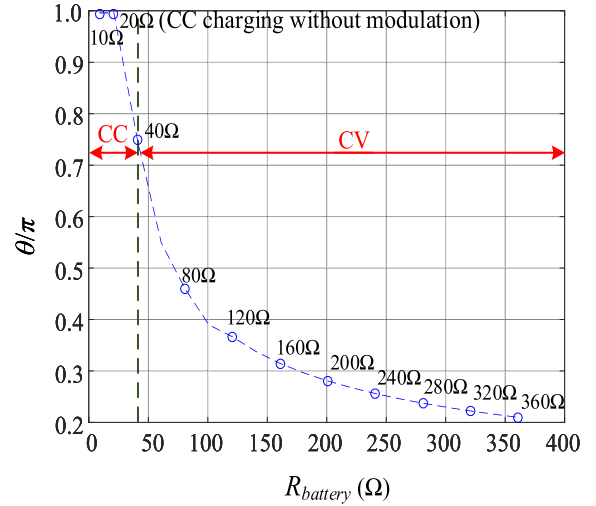

Fig. 8. (a) Simulation points of phase shift angle θ versus battery resistance. (b) Simulation points of conduction angle α versus battery resistance.
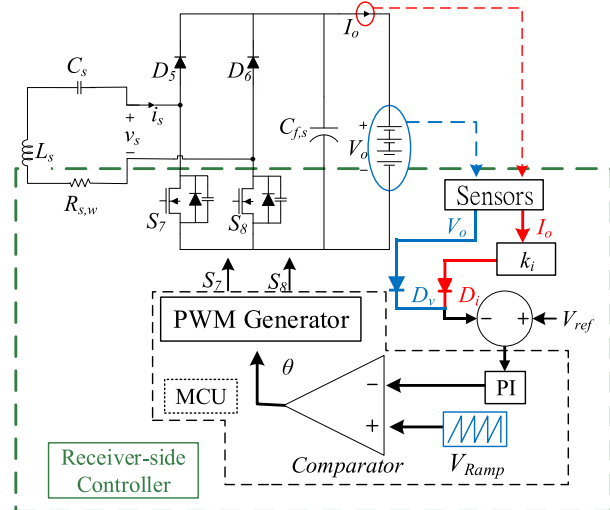

Fig. 9. Control diagram of SAR at receiver side.

charging stage, which will be discussed in Section IV-C in detail.

B. CV Charging

In order to comply with the CV charging profile as shown in Fig. 1, keeping the operating frequency of the inverter at a constant ω_p, the charging current I_O will decrease with time. The conduction angle θ of the SAR can be tuned within $[0, \pi]$. Thus, a controllable I_O can be achieved as

$$I_O = \frac{2}{\pi} \sin^2\left(\frac{\theta}{2}\right)|\boldsymbol{I}_s| \qquad (24)$$

$$\boldsymbol{I}_s \approx \frac{4}{\pi} \frac{\boldsymbol{V}_p}{\omega_p M}. \qquad (25)$$

Along with decreasing θ and increasing R_{Battery}, I_O can be regulated to maintain a constant V_O. According to (6), a load reactance will be generated with the modulation of θ. With the analysis in Section III-B, X_{eq} will degrade the efficiency performance as the extent of modulated phase shift angle θ increases, that is, θ decreases. To address this problem, phase shift PWM is adopted in the inverter to modulate the input voltage magnitude, which can indirectly regulate the output voltage. By increasing α, the magnitude of $\boldsymbol{V}_p$ will be decreased. Thereby, I_S will be decreased due to the decreasing of $\boldsymbol{V}_p$. As shown in (24) and (25), except θ, I_O also can be adjusted by changing the magnitude of $\boldsymbol{V}_p$, thus relaxing the extent of modulated phase shift angle θ, in other words reducing the created load reactance, X_{eq}, given by

$$|\boldsymbol{V}_p| = \frac{4}{\pi}V_I \cos\left(\frac{\alpha}{2}\right). \qquad (26)$$

To keep soft switching in the inverter, α should be smaller than the input phase angle β of the IPT converter, which can be calculated by

$$\alpha \leq \beta = \frac{1}{\pi} \arctan\left|\frac{\text{Im}(Z_{\text{in}})}{\text{Re}(Z_{\text{in}})}\right|. \qquad (27)$$

To minimize the extent of the extent of modulated phase shift angle θ for efficiency optimization, the modulated conduction angle α should be maximized, that yields

$$\alpha = \beta. \qquad (28)$$

With (24)–(26), the operating points for CV charging are shown in Fig. 8. From the CV charging state in Fig. 8, with increasing R_{Battery} from 40 to 360 Ω during the charging process, the value of phase shift angle θ at SAR will keep decreasing. Meanwhile, the modulated conduction angle α at the inverter will increase to relax the decreasing of θ, which reduces the X_{eq}.

C. Control Schemes of Both Sides

With the operation principles for CC and CV charging for the IPT converter discussed in Sections IV-A and IV-B, respectively, the inverter at the transmitter side and the SAR at the receiver side can be independently controlled without the necessary of feedback wireless communication between them. As shown in Fig. 9, the receiver-side controller detects the charging information V_O and I_O. Here, $k_i = (V_{\text{Rated}}/I_{\text{Rated}})$ where I_{rated} is the rated current of the battery. During the initial of CC charging stage, since V_o is lower than V_{rated} ($V_O < I_O k_i$)
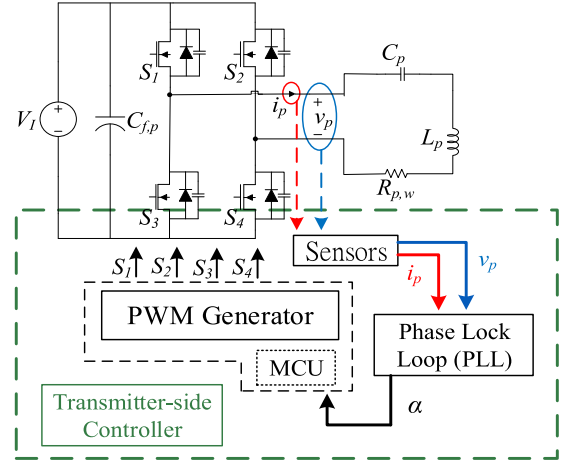

Fig. 10. Control diagram of inverter at transmitter side.

causes that the diode D_i is on and diode D_v is reversed biased, the red control path will be operated in the receiver-side controller. Thus, I_O is regulated at the required I_{Rated}. Since the constant output current in SSIPT converter can be achieved under alignment case, the SAR can be operated as a passive rectifier without modulation. Meanwhile, V_O gradually increases until it reaches the required rated voltage V_{Rated}, which means CC charging stage is completed. At the initial CV charging stage, I_O starts to decrease ($V_O > I_O k_i$), which causes that the diode D_v is on and diode D_i is reversed biased. The converter will enter into CV charging stage and the blue control path will be activated, V_O is regulated at the required V_{Rated}. Thus, the transition from CC charging stage to CV charging stage can be achieved.

For both CC and CV charging control, first of all, the signal $I_O k_i$ or V_O is subtracted from the reference voltage V_{ref}. After that, this difference signal is compared with a fixed switching frequency triangular carrier wave to output phase shift angle θ based on (24). Then the microcontroller MCU will output the corresponding conduction angle of the SAR in order to directly regulate the output current I_O. θ is approximately equal to π during CC charging mentioned as discussed in Section IV-A. Once V_O reaches the threshold charging voltage value, θ will be automatically decreased to comply with the CV charging profile. Due to the direct control of the SAR by the receiver-side controller without the necessity of wireless communication with the transmitter side, the charging safety and fast response can be ensued.

As shown in Fig. 10, the transmitter-side controller can simply fix the operating frequency of the inverter and modulates the conduction angle α close to its maximum value in (28), while soft switching of inverter can be guaranteed. The input phase angle β between i_P and v_P is caused by the control of the phase shift angle θ of the SAR. As shown in (28), α is designed to be equal to β. Since α can be detected by using a phase lock loop (PLL) circuit and can be directly outputted by another MCU at the transmitter side, thus the phase shift PWM driving signals for the inverter can be generated without the necessity of getting the information from the receiver side.

TABLE III
SIMULATION PARAMETERS

Symbol	Parameters	Measured Values
I_O	Rated charging current	5A
V_O	Rated charging voltage	170V
V_I	Input dc voltage	155.5V
L_P, L_S	Self-inductance	256µH, 364µH
C_P, C_S	Compensated capacitance	40nF, 22nF
k	Coupling coefficient	0.255
$R_{P,w}, R_{S,w}$	Coil resistance	0.4Ω, 0.8Ω
$f_{operating}$	Operating frequency	50kHz

TABLE IV
EXPERIMENTAL PARAMETERS

Symbol	Parameters	Measured Values
I_O	Rated charging current	5 A
V_O	Rated charging voltage	170V
V_I	Input DC voltage	155.5V
S_1-S_4	Switches	SCT3022AL with
S_7, S_8		$R_{on} \approx 22m\Omega$, $V_F \approx 3.2V$
D_5, D_6	Diodes	FFSH5065A with $V_F \approx 1.51V$
L_P, L_S	Self-inductance	255.5µH, 364.4µH
C_P, C_S	Compensated capacitance	39.8nF, 26.8nF
k	Coupling coefficient	0.255
$R_{P,w}, R_{S,w}$	Coil resistance	0.35Ω, 0.95Ω
$f_{operating}$	Operating frequency	50kHz

From Fig. 10, the MCU at the transmitter side can tune α value in order to achieve its maximum value.

Under misalignment cases, during CC charging, the SAR is not operating as a passive rectifier anymore but operates with the same control strategy as the CV charging stage as discussed above. The only difference is the regulated goal, I_O for CC charging stage and V_O for CV charging stage. During CV charging, the control strategy remains changed even under misalignment cases.

With the proposed control scheme in Figs. 9 and 10, the IPT converter can eliminate the feedback wireless communication requirement and achieve direct and safe output regulation.

D. Stability Analysis of Control Strategy

Since the control of θ at SAR is faster than the control of α at the inverter, it can be assumed that transmitter-side controller and receiver-side controller operate separately for simplicity. As a zero-crossing detection of PLL at the transmitter side is open-loop, the stability of transmitter controller is guaranteed by a stable dc input voltage V_I.

1) CC Charging Mode: Inherent CC output characteristic of the SSIPT converter has applied for the design of the CC charging stage. During CC charging under alignment case, the receiver side operates as a passive rectifier, which can be modeled as Fig. 5.

From (9) and (10), the relation between I_s and V_p can be realized as

$$I_s = \frac{j\omega M}{\left(Z_{eq} + Z_s\right)\left(Z_p + \frac{\omega^2 M^2}{Z_s + Z_{eq}}\right)} V_p. \quad (29)$$

Thus, for changing the coordinate by using the frequency shift theorem of Laplace transform [42], the s-domain equivalent impedance of the SSIPT converter system can be described by the following transfer function:

$$I_S(s) = \frac{(s - j\omega)M}{\left(Z_{eq}(s) + Z_S(s)\right)\left(Z_P(s) + \frac{\omega^2 M^2}{Z_S(s) + Z_{eq}(s)}\right)} V_P(s). \quad (30)$$

The stability of the SSIPT system can be realized by the pole-zero map of the equivalent impedance. The load range of CC charging stage is [0 Ω, 40 Ω]. With the help of the experimental parameters in Table IV, the pole-zero map of the SSIPT system under different load conditions is given in
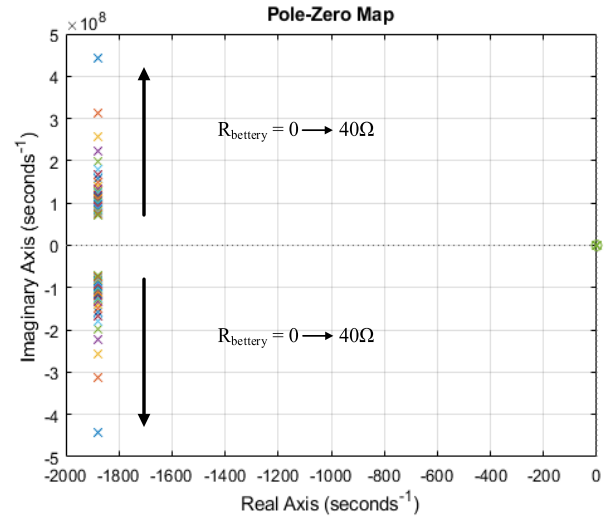

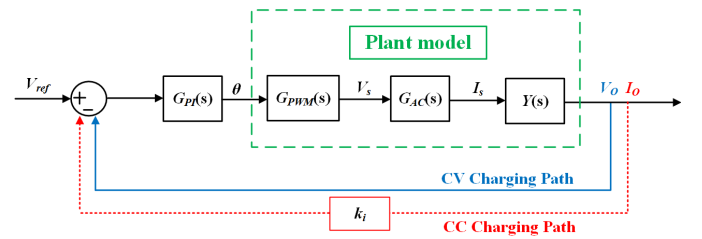Fig. 11. Pole-zero map of the SSIPT system at load range of CC charging stage from 0 to 40 Ω.

Fig. 12. Control block diagram of the receiver-side controller.

Fig. 11. It indicates that the system poles stay at the left-hand side of the complex plane, which are far away from the imaginary axis. However, it is obviously realized that the designed SSIPT system is stable under the load range of CC charging stage. Moreover, the misalignment case during CC charging is inevitable. According to the discussion in Section IV-C, the same controller for the receiver side CC and CV charging is used; the only difference among them is the sensed signal with its gain. The control scheme of CC charging under misalignment case is represented as red path in Fig. 12.

2) CV Charging Mode: For the CV charging stage, the SSIPT itself cannot achieve the load-independent output voltage. Thus, a feedback voltage controller is necessary to be used at the receiver side. According to the control scheme at the receiver side, the control block diagram of the receiver-side controller is given in Fig. 12, where the transfer functions are described in the following.

The PI controller is tuned by the Ziegler–Nichols' rules [43]. $G_{\text{PI}}(s)$ is the transfer function of the PI controller, which is given as

$$G_{\text{PI}}(s) = K\left(1 + \frac{1}{\tau_I s}\right) \tag{31}$$

where K is the control gain and τ_I is the integrator time constant

$$K = \frac{1}{2.2|G_{\text{Plant}}(j\omega)|} \tag{32}$$

$$\tau_I = \frac{2\pi}{1.2\omega}. \tag{33}$$

The plant model of receiver side can be realized by $G_{\text{Plant}}(s) = G_{\text{PWM}}(s)G_{\text{AC}}(s)Y(s)$. $G_{\text{PWM}}(s)$ is the small-signal transfer function of the PWM process, which can be modeled as a time delay [44]

$$G_{\text{PWM}}(s) = e^{-1.5T_s s} \tag{34}$$

where T_s is the sampling period.

From Fig. 5, the receiver-side ac current $I_s(s)$ can be obtained as

$$I_s(s) = \frac{1}{Z_s(s)}V_s(s) - \frac{1}{Z_s(s)}sMI_p(s). \tag{35}$$

$G_{\text{AC}}(s)$ is the transfer function between V_s and I_s (ac circuit part at receiver side), which is given as

$$G_{\text{AC}}(s) = \frac{1}{Z_s(s)}. \tag{36}$$

$Y(s)$ is the small-signal model of the dc circuit part at receiver side, which is the transfer function from I_s to V_o. This model has considered the output capacitor $C_{f,s}$ and the load resistance R_{battery} [44]. The relationship between I_s (s) and V_o (s) can be derived as

$$I_S(s) = Y(s)V_O(s) \tag{37}$$

where $Y(s)$ can be realized as

$$Y(s) = \frac{1}{V_{\text{ref}}C_{f,s}s + \frac{V_{\text{ref}}^2}{R_{\text{battery}}}}. \tag{38}$$

The small-signal stability can also be realized from the pole-zero map of the closed-loop system, in which the closed-loop transfer function can be derived as

$$G_{\text{CL}}(s) = \frac{G_{\text{PI}}(s)G_{\text{PWM}}(s)G_{\text{AC}}(s)Y(s)}{1 + G_{\text{PI}}(s)G_{\text{PWM}}(s)G_{\text{AC}}(s)Y(s)}. \tag{39}$$

With the help of the experimental parameters in Table IV and (39), the pole-zero map of the closed-loop system at load range of CV charging stage from 40 to 360 Ω is given in Fig. 13. From Fig. 13, the closed-loop system poles of CV charging stage stay at the left-hand side of the complex plane, which means that the closed-loop controlled IPT system is stable at load range of CV charging stage from 40 to 360 Ω.
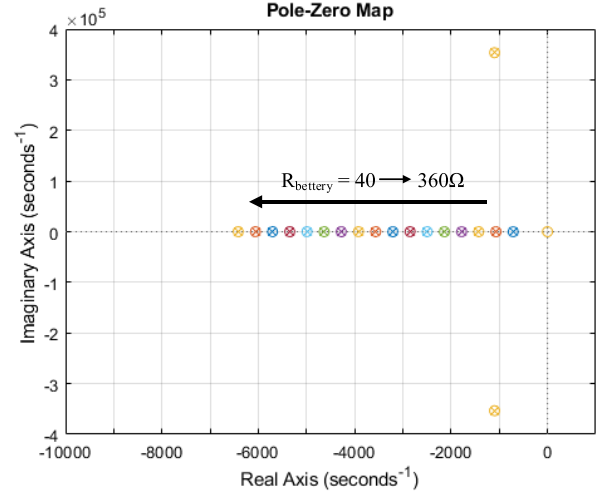

Fig. 13. Pole-zero map of the closed-loop system at the load range of CV charging stage from 40 to 360 Ω.
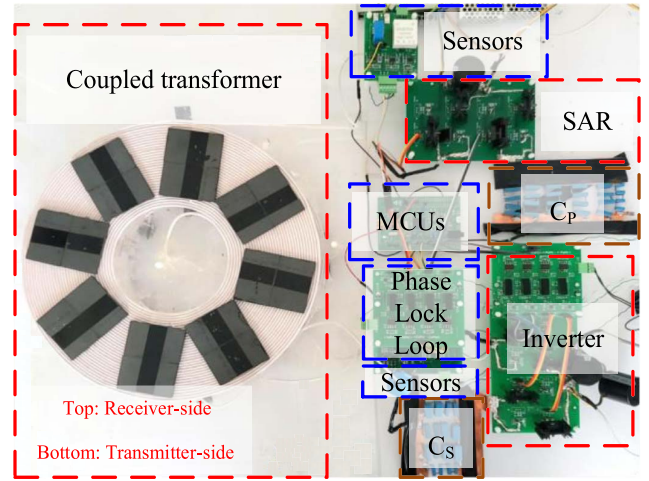

Fig. 14. 1-kW experimental SS IPT prototype.

V. EXPERIMENTAL VERIFICATION

A. Specifications and Experimental Prototype

To verify the CC and CV charging of the SSIPT with a constant frequency and without feedback wireless communication, an experimental prototype was built in the laboratory as shown in Fig. 14, and its corresponding parameters are given in the Table IV. In the experiment, the electronic load is used to emulate the battery, with the load ranges from 20 to 335 Ω. The input and output dc powers are measured by Yokogawa WT1800 Digital Power Analyzer, and the experimental waveforms are captured by the Yokogawa DL850EV Power Scope.

B. Measured Operating Points, Charging Process and Waveforms

The proposed CC and CV operation principles of the SSIPT converter discussed in Section IV is studied and evaluated via the experimental prototype as in Fig. 14. The proposed system including the inverter part and SAR part operates
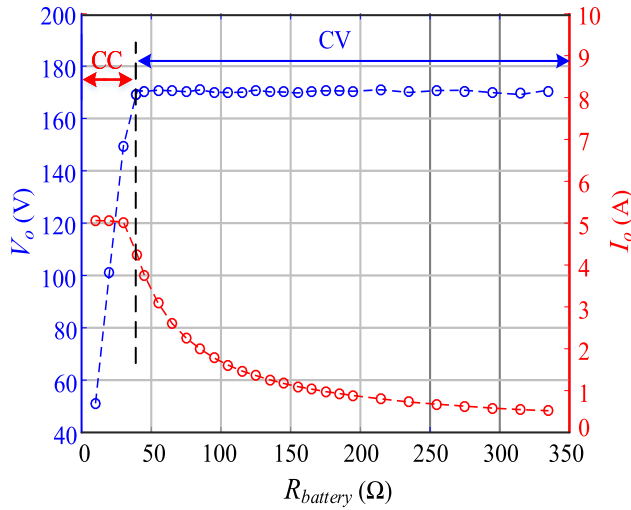
Fig. 15.   Measured output points of output charging current I_O and voltage V_O for whole charging process versus battery resistance.

Fig. 16.   Measured operating points of conduction angle α and phase shift angle θ at constant operating frequency.

at a constant operating frequency of 50 kHz during the whole charging process. The SAR at the receiver side is responsible for direct output voltage regulation by varying its conduction angle, while the inverter at the transmitter side are independently controlled to achieve an efficient charging profile through relaxing the extent of modulated phase shift angle of SAR at the receiver side. By adjusting the conduction angle of the inverter and the phase shift angle of the SAR, the SSIPT converter can achieve precise output and efficiency enhancement during the whole charging process without the necessary of feedback wireless communication.

During the CC charging stage, the inverter operates at 50 kHz. The phase shift angle of the SAR is fixed at π for inherent LIC output for CC charging and the conduction angle of the inverter is fixed at zero as discussed in Section IV-A. The measured output points are shown in Fig. 15 which highlighted in red. Obviously, the charging output current approximately keeps constant at 5 A during CC charging stage, in which the charging voltage increases until it reaches the threshold charging voltage of 170 V.

Then, the charging system transits into CV charging stage. The SAR is tightly regulated to control the output voltage to track the constant charging voltage of 170 V, while the inverter is still operating at a fixed 50 kHz and independently controlled to minimize the input magnitude by phase shift PWM, in order to minimize the extent of the extent of modulated phase shift angle θ of the SAR for efficiency optimization as discussed in Section IV-B. The measured output points and the operating points are plotted as shown in Figs. 15 and 16, respectively. As shown in Fig. 16, along with the charging process, the conduction angle α of the inverter increases while the phase shift angle θ of the SAR decreases. In detail, by increasing R_{Battery} varied from 40 to 355 Ω, the phase shift angle θ varies from 0.780π to 0.296π and the conduction angle α varies from 0.166π to 0.596π. Compared with the simulation results, their trends are consistent.
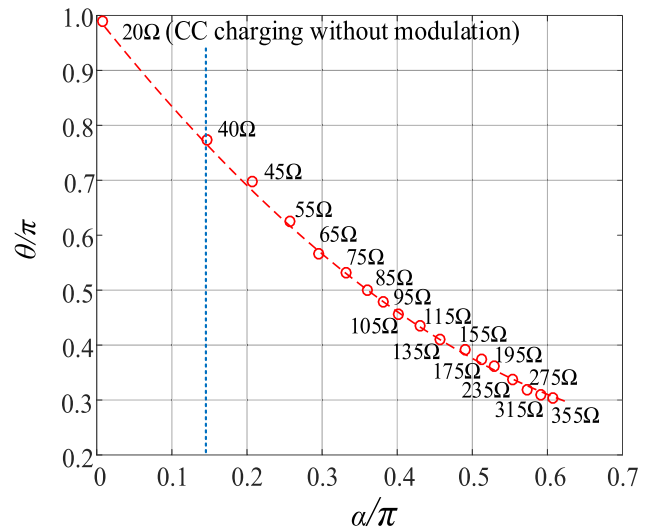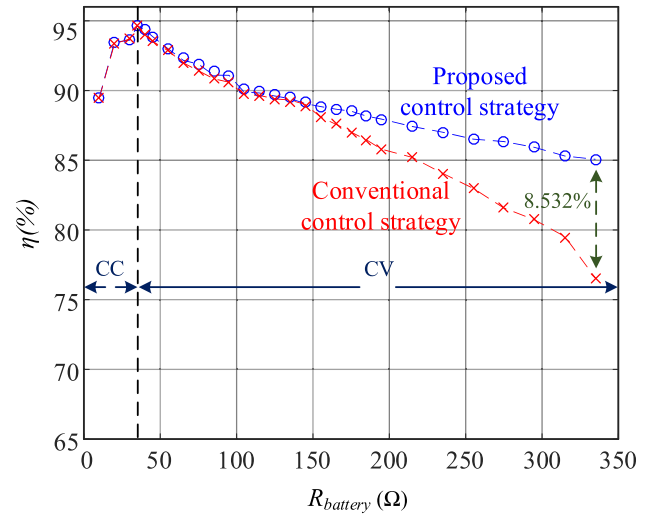

Fig. 17.   Measured charging efficiency of the proposed approach and the conventional approach [14].

The comparison of the efficiency between the proposed control strategy and the conventional control strategy [14] for the SSIPT is shown in Fig. 17. The conventional control method applies various operating frequency for tracking the LIV output with feedback wireless communication [14]. From Fig. 17, the proposed control method can keep the efficiency over 85%, which is better than the conventional one for the CV charging stage. The proposed one can obtain an efficiency of 8.536% better than the conventional one at the end of charging.

With the proposed control strategy of the IPT converter, the experimental waveforms of inverter and SAR at CC charging with $R_{\text{battery}} = 20$ Ω, initial period of CV charging with $R_{\text{battery}} = 40$ Ω, and the end of CV charging with $R_{\text{battery}} = 335$ Ω, are shown in Fig. 18(a)–(c), respectively. From Fig. 18, it obviously shows that the ZVS can be achieved in both inverter and SAR parts. Fig. 20 shows that the transient voltage and current of the switch S_1 and S_4 at $R_{\text{battery}} = 20$ Ω
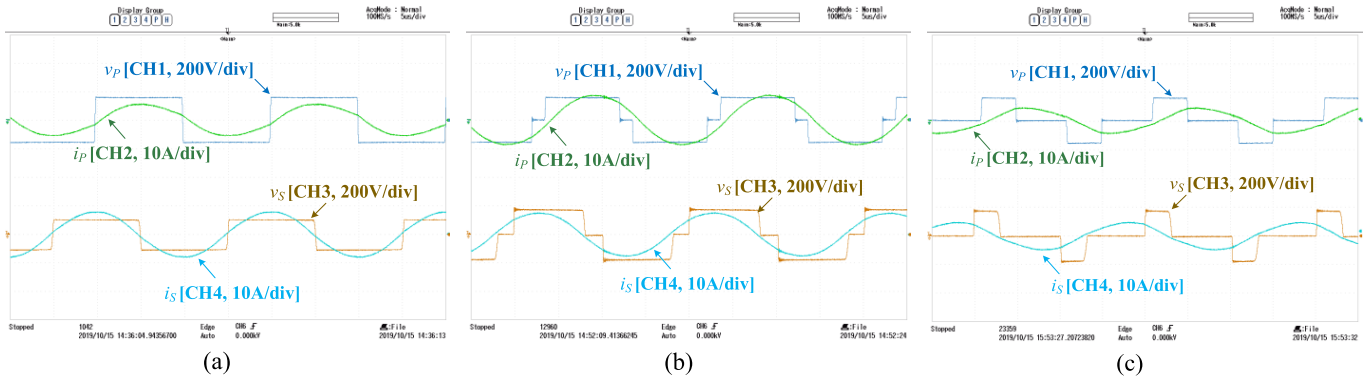
Fig. 18. Measured operating waveforms of the inverter and SAR at (a) CC charging, (b) initial period of CV charging, and (c) end of CV charging.
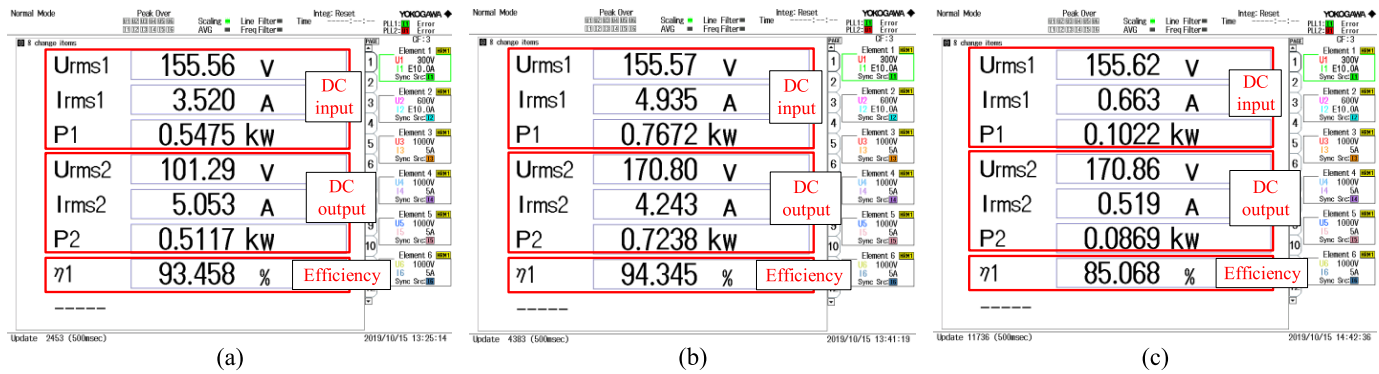

Fig. 19. Screen capture of experimental input power, output power and efficiency at (a) CC charging, (b) initial period of CV charging, and (c) end of CV charging.

during CC charging (S_2 and S_3 have the same results) as an example. v_{ds} is the voltage across the drain-to-source of a MOSFET, while i_{ds} is the drain-to-source current of a MOSFET. When the S_1 and S_4 are turned on (the gate signals go high), their voltage v_{ds} become 0. As v_{ds} is much lower than the forward–on voltage of the body diode therefore current naturally commutates from the body diodes to the device's channels and ZVS is achieved. As the current i_{ds} is still negative at this moment, S_1 and S_4 are turned on with a reverse current, which means the current goes through their anti-parallel diodes instead of the MOSFET itself. Therefore, ZVS can be achieved if the i_{ds} is reversed or in negative value [45]. From the turn-on instance of Fig. 20, S_1 and S_4 are turned on while their i_{ds} are reversed. Thus, the ZVS of the inverter can be achieved even if it is without modulation during CC charging under alignment case. Moreover, Fig. 21(a) and (b) shows that the transient voltage and current of the switch S_1 and S_4 (S_2 and S_3 will have the same results) and S_7(S_8 has the same result) at $R_{battery} = 335\ \Omega$ during CV charging stage, respectively. From the turn-on instant of Fig. 21(a) and (b), S_1, S_4 and S_7 are turned on while their i_{ds} are reversed [45]. Thus, they verify that both the inverter part and SAR part can achieve soft switching during CV charging stage. Also, the corresponding screen capture of the experimental input power, output power and efficiency are shown in Fig. 19(a)–(c), respectively. In summary, the proposed control strategy can satisfy the charging requirement of the battery efficiently
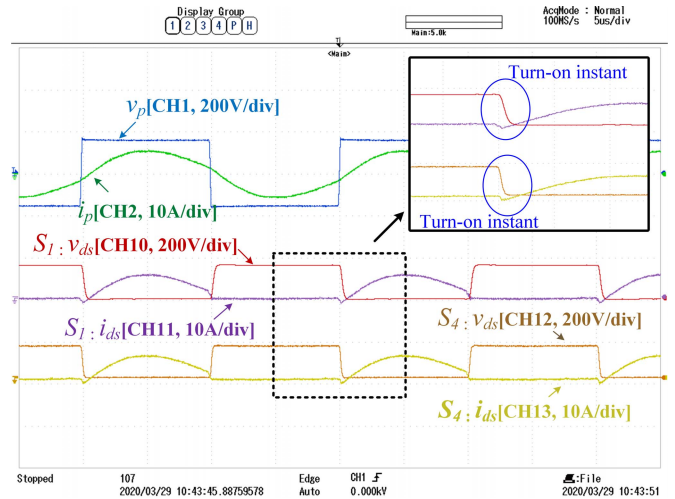
Fig. 20. Transient voltage and current of the switches S_1 and S_4 at $R_{battery} = 20\ \Omega$ during CC charging stage under ideal alignment case.

for the whole charging process with a constant operating frequency and without the necessity of wireless communication between transmitter and receiver sides.

C. Transient Response for Variations of Load

A closed-loop controller has been implemented for the SSIPT experimental platform for CV charging. And the
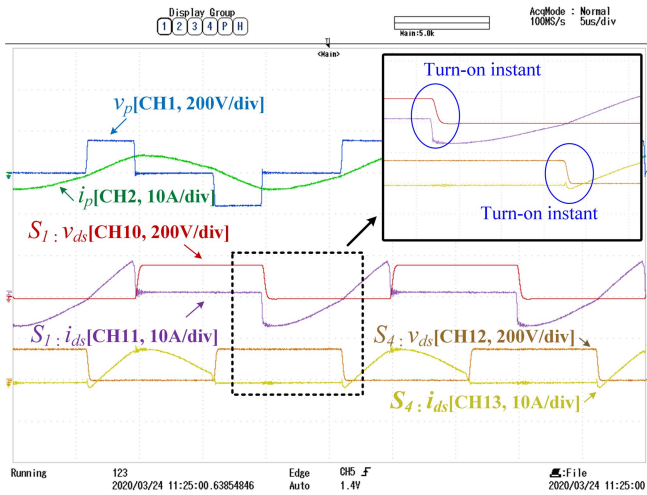
(a)

(b)

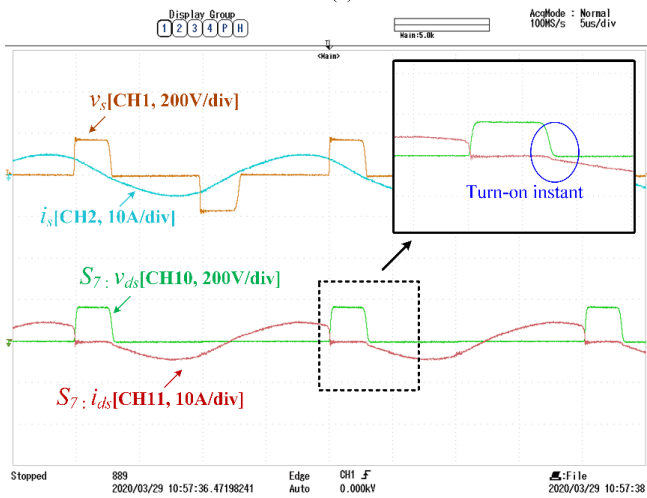Fig. 21. (a) Transient voltage v_{ds} and current i_{ds} of the switches S_1 and S_4 at $R_{battery} = 335$ Ω during CV charging. (b) Transient voltage and current of the switches S_7 at $R_{battery} = 335$ Ω during CV charging stage.
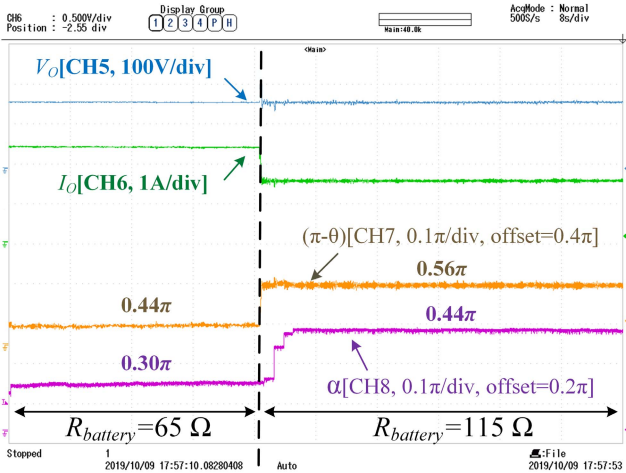

Fig. 22. Transient waveforms (V_o, I_o, π-θ, α) when $R_{battery}$ steps change from 65 to 115 Ω.

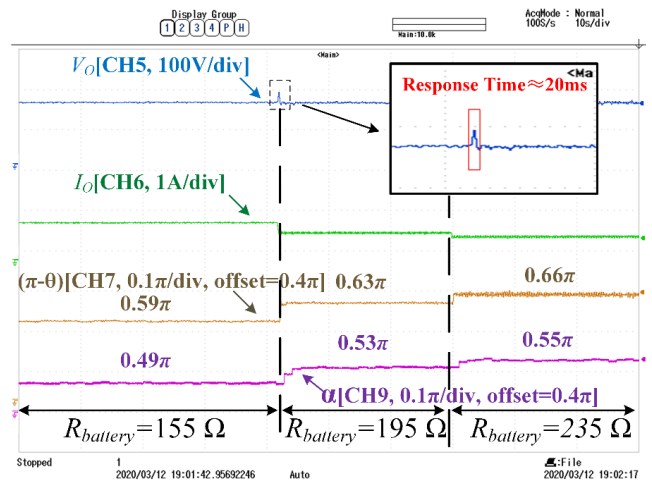experimental transient waveforms of the charging output voltage V_O and current I_O from a load step change from 65 to

Fig. 23. Transient waveforms (V_o, I_o, π-θ, α) when $R_{battery}$ steps change from 155 to 195 Ω and then to 235 Ω.
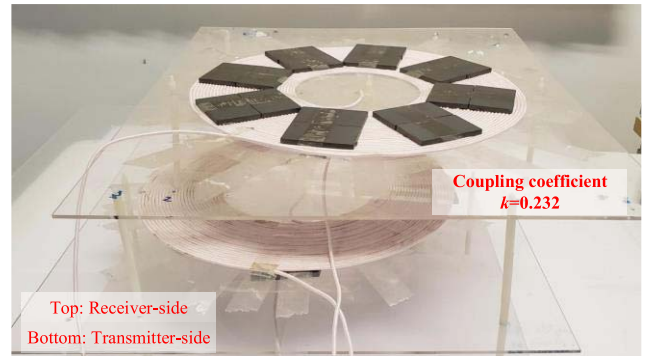

Fig. 24. Experimental coils with misalignment, coupling coefficient $k = 0.232$.

115 Ω are shown in Fig. 22. The output voltage V_O is shown in CH5 and the output current I_O is shown in CH6. Also, the conduction angle π-θ for the SAR and the conduction angle α for the inverter are shown in CH7 and CH8. During the control process, θ is directly controlled for output voltage regulation, while α is adjusted correspondingly based on the changing of θ. Moreover, Fig. 23 shows a continuous load step change for a larger load range, from 155 to 235 Ω in which CH7 and CH9 show the conduction angle π-θ of the SAR and conduction angle α of the inverter. Also, the response time of the control strategy is also shown in Fig. 23, which is about 20 ms. Figs. 22 and 23 indicate that the SSIPT converter is stable within the charging load range. Compared with the control of θ, control of α is slower. Since the charging process is slow, the proposed control strategy can satisfy the charging requirement. In addition, no feedback wireless communication technique is needed during the whole charging process.

D. Misalignment Effect

Misalignment issues are inevitable in wireless battery charging because of charging positioning error, causing the unexpected output current or voltage. When the coupling coefficient k changes from 0.255 to 0.232 as shown in Fig. 24
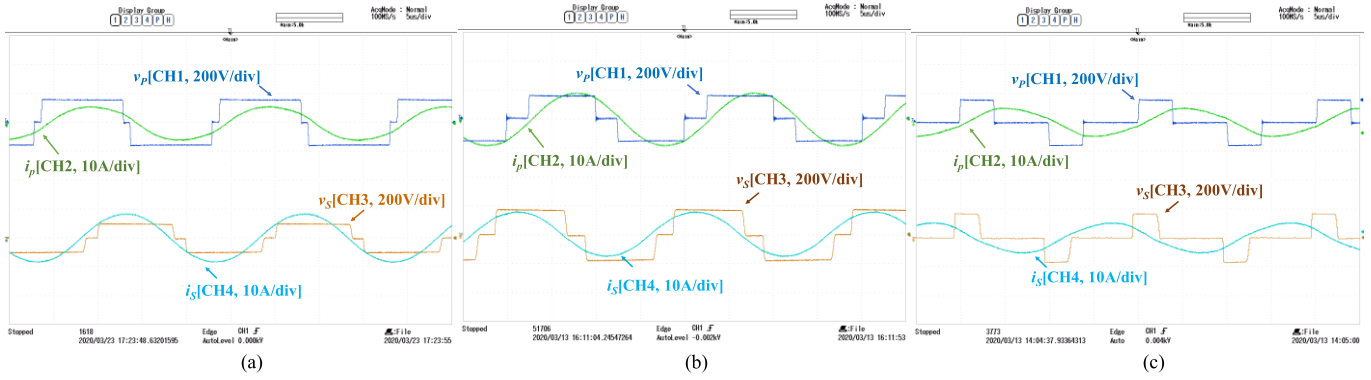
Fig. 25. Measured operating waveforms of the inverter and SAR at (a) CC charging, (b) initial period of CV charging, and (c) end of CV charging under misalignment, $k = 0.232$.
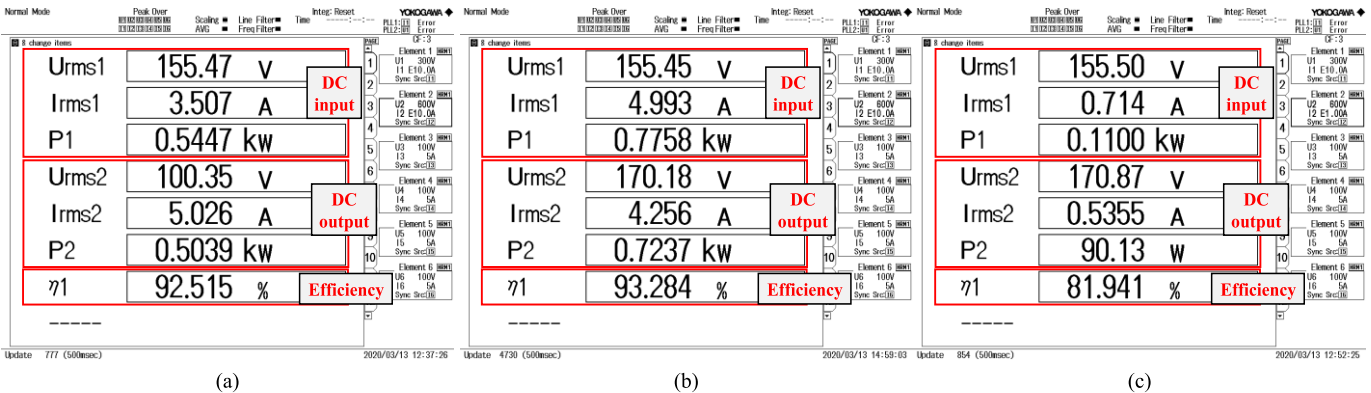
Fig. 26. Screen capture of experimental input power, output power and efficiency at (a) CC charging, (b) initial period of CV charging, and (c) end of CV charging under misalignment, $k = 0.232$.
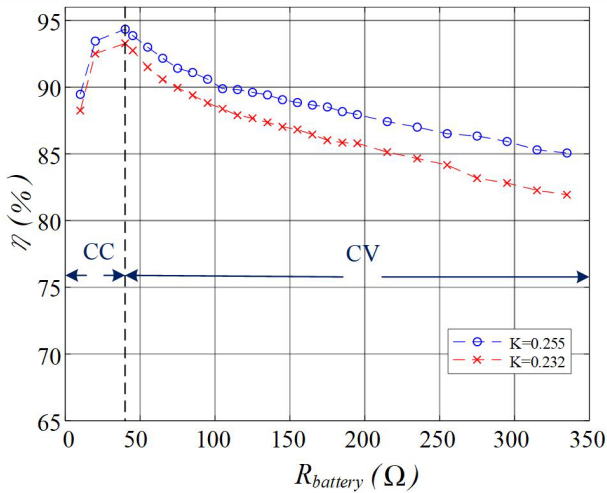
Fig. 27. Comparison of measured charging efficiency of the proposed approach under $k = 0.255$ and $k = 0.232$.

Fig. 28. Comparison of measured operating points of conduction angle α and phase shift angle θ at constant operating frequency under $k = 0.255$ and $k = 0.232$.

due to misalignment, Fig. 25 shows the measured operating waveforms of the inverter and SAR with misalignment $k = 0.232$ at CC charging stage with $R_{\text{battery}} = 20 \ \Omega$, initial period of CV charging stage with $R_{\text{battery}} = 40 \ \Omega$, and the end of CV charging stage with $R_{\text{battery}} = 335 \ \Omega$. From Fig. 25, the output current regulation is achieved by the SAR. Compared Fig. 26 with Fig. 19, the constant output current

and constant output voltage characteristics can be kept almost constant even under misalignment. Moreover, the operation phase shift and conduction angle of θ and α under $k = 0.255$ and $k = 0.232$ are shown in Fig. 28, while their corresponding charging efficiency curves are given in Fig. 27. Finally, from Figs. 25–28, the proposed control modulation techniques for the SSIPT converter can relax the misalignment

effect, achieving the constant output current and voltage and still maintaining high efficiency.

VI. Conclusion

This paper reported a constant-frequency non-communication-based control method for IPT converters. Verified by a single-stage SS IPT battery charger, both CC and CV charging profiles are underpinned by controlling the phase shift angle of the SAR, and the conduction angle of the inverter. A constant operating frequency and no feedback wireless communication aid lowering the risk of instability during charging while improving the charging efficiency. Also, it allows no extra dc–dc converter and power switch to save cost. Fully soft switching with simple control results in high efficiency at both the receiver and transmitter sides. Compared with the typical variable-frequency charging approach, a better efficiency is demonstrated here with respect to both theoretical analysis and experimental verification.

References

[1] A. Khaligh and Z. Li, "Battery, ultracapacitor, fuel cell, and hybrid energy storage systems for electric, hybrid electric, fuel cell, and plug-in hybrid electric vehicles: State of the art," *IEEE Trans. Veh. Technol.*, vol. 59, no. 6, pp. 2806–2814, Jul. 2010.

[2] H. Hoang, S. Lee, Y. Kim, Y. Choi, and F. Bien, "An adaptive technique to improve wireless power transfer for consumer electronics," *IEEE Trans. Consum. Electron.*, vol. 58, no. 2, pp. 327–332, May 2012.

[3] Q. Li and Y. C. Liang, "An inductive power transfer system with a high-Q resonant tank for mobile device charging," *IEEE Trans. Power Electron.*, vol. 30, no. 11, pp. 6203–6212, Nov. 2015.

[4] U. K. Madawala and D. J. Thrimawithana, "A bidirectional inductive power interface for electric vehicles in V2G systems," *IEEE Trans. Ind. Electron.*, vol. 58, no. 10, pp. 4789–4796, Oct. 2011.

[5] G. A. Covic and J. T. Boys, "Inductive power transfer," *Proc. IEEE*, vol. 101, no. 6, pp. 1276–1289, Jun. 2013.

[6] T. Imura and Y. Hori, "Maximizing air gap and efficiency of magnetic resonant coupling for wireless power transfer using equivalent circuit and Neumann formula," *IEEE Trans. Ind. Electron.*, vol. 58, no. 10, pp. 4746–4752, Oct. 2011.

[7] C. Duan, C. Jiang, A. Taylor, and K. Bai, "Design of a zero-voltage-switching large-air-gap wireless charger with low electrical stress for Plugin hybrid electric vehicles," in *Proc. IEEE Transp. Electrific. Conf. Expo (ITEC)*, Detroit, MI, USA, Jun. 2013, pp. 1–5.

[8] W. X. Zhong and S. Y. R. Hui, "Maximum energy efficiency tracking for wireless power transfer systems," *IEEE Trans. Power Electron.*, vol. 30, no. 7, pp. 4025–4034, Jul. 2015.

[9] M. Fu, C. Ma, and X. Zhu, "A cascaded Boost–Buck converter for high-efficiency wireless power transfer systems," *IEEE Trans. Ind. Informat.*, vol. 10, no. 3, pp. 1972–1980, Aug. 2014.

[10] M. Fu, H. Yin, X. Zhu, and C. Ma, "Analysis and tracking of optimal load in wireless power transfer systems," *IEEE Trans. Power Electron.*, vol. 30, no. 7, pp. 3952–3963, Jul. 2015.

[11] T.-D. Yeo, D. Kwon, S.-T. Khang, and J.-W. Yu, "Design of maximum efficiency tracking control scheme for closed-loop wireless power charging system employing series resonant tank," *IEEE Trans. Power Electron.*, vol. 32, no. 1, pp. 471–478, Jan. 2017.

[12] X. Qu, H. Han, S.-C. Wong, C. K. Tse, and W. Chen, "Hybrid IPT topologies with constant current or constant voltage output for battery charging applications," *IEEE Trans. Power Electron.*, vol. 30, no. 11, pp. 6329–6337, Nov. 2015.

[13] R. Mai, Y. Chen, Y. Li, Y. Zhang, G. Cao, and Z. He, "Inductive power transfer for massive electric bicycles charging based on hybrid topology switching with a single inverter," *IEEE Trans. Power Electron.*, vol. 32, no. 8, pp. 5897–5906, Aug. 2017.

[14] Z. Huang, S.-C. Wong, and C. K. Tse, "Design of a single-stage inductive-power-transfer converter for efficient EV battery charging," *IEEE Trans. Veh. Technol.*, vol. 66, no. 7, pp. 5808–5821, Jul. 2017.

[15] V.-B. Vu, D.-H. Tran, and W. Choi, "Implementation of the constant current and constant voltage charge of inductive power transfer systems with the double-sided LCC compensation topology for electric vehicle battery charge applications," *IEEE Trans. Power Electron.*, vol. 33, no. 9, pp. 7398–7410, Sep. 2018.

[16] Z. Huang, S.-C. Wong, and C. K. Tse, "Control design for optimizing efficiency in inductive power transfer systems," *IEEE Trans. Power Electron.*, vol. 33, no. 5, pp. 4523–4534, May 2018.

[17] Z. Huang, S.-C. Wong, and C. K. Tse, "Comparison of basic inductive power transfer systems with linear control achieving optimized efficiency," *IEEE Trans. Power Electron.*, vol. 35, no. 3, pp. 3276–3286, Mar. 2020.

[18] T. Diekhans and R. W. De Doncker, "A dual-side controlled inductive power transfer system optimized for large coupling factor variations and partial load," *IEEE Trans. Power Electron.*, vol. 30, no. 11, pp. 6320–6328, Nov. 2015.

[19] Y. Jiang et al., "Double-side phase shift control for impedance matching in wireless high power transfer," in *Proc. IEEE Energy Convers. Congr. Exposit. (ECCE)*, Baltimore, MD, USA, Sep. 2019, pp. 3368–3373.

[20] C. Wang, M. Chen, H. Cui, X. Liu, W. Zhong, and F. Shi, "A novel soft-switching dual-side phase shift circuit for wireless power transfer," in *Proc. IEEE Energy Convers. Congr. Exposit. (ECCE)*, Baltimore, MD, USA, Sep. 2019, pp. 5344–5351.

[21] Z. Huang, S.-C. Wong, and C. K. Tse, "An inductive-power-transfer converter with high efficiency throughout battery-charging process," *IEEE Trans. Power Electron.*, vol. 34, no. 10, pp. 10245–10255, Oct. 2019.

[22] C. Zheng et al., "High-efficiency contactless power transfer system for electric vehicle battery charging application," *IEEE J. Emerg. Sel. Topics Power Electron.*, vol. 3, no. 1, pp. 65–74, Mar. 2015.

[23] K. Song, Z. Li, J. Jiang, and C. Zhu, "Constant current/voltage charging operation for series–series and series–parallel compensated wireless power transfer systems employing primary-side controller," *IEEE Trans. Power Electron.*, vol. 33, no. 9, pp. 8065–8080, Sep. 2018.

[24] M. Huang, Y. Lu, and R. P. Martins, "A reconfigurable bidirectional wireless power transceiver for battery-to-battery wireless charging," *IEEE Trans. Power Electron.*, vol. 34, no. 8, pp. 7745–7753, Aug. 2019.

[25] E. Gati, G. Kampitsis, and S. Manias, "Variable frequency controller for inductive power transfer in dynamic conditions," *IEEE Trans. Power Electron.*, vol. 32, no. 2, pp. 1684–1696, Feb. 2017.

[26] K. N. Mude, "Battery charging method for electric vehicles: From wired to on-road wireless charging," *Chin. J. Electr. Eng.*, vol. 4, no. 4, pp. 1–15, Dec. 2018.

[27] Y. Jiang, L. Wang, Y. Wang, J. Liu, M. Wu, and G. Ning, "Analysis, design, and implementation of WPT system for EV's battery charging based on optimal operation frequency range," *IEEE Trans. Power Electron.*, vol. 34, no. 7, pp. 6890–6905, Jul. 2019.

[28] Y. Jiang, L. Wang, Y. Wang, J. Liu, X. Li, and G. Ning, "Analysis, design, and implementation of accurate ZVS angle control for EV battery charging in wireless high-power transfer," *IEEE Trans. Ind. Electron.*, vol. 66, no. 5, pp. 4075–4085, May 2019.

[29] Q. Chen, L. Jiang, J. Hou, X. Ren, and X. Ruan, "Research on bidirectional contactless resonant converter for energy charging between EVs," in *Proc. 39th Annu. Conf. IEEE Ind. Electron. Soc. (IECON)*, Vienna, Austria, Nov. 2013, pp. 1236–1241.

[30] Z. Huang, C.-S. Lam, P.-I. Mak, R. P. D. S. Martins, S.-C. Wong, and C. K. Tse, "A single-stage inductive-power-transfer converter for constant-power and maximum-efficiency battery charging," *IEEE Trans. Power Electron.*, vol. 35, no. 9, pp. 8973–8984, Sep. 2020, doi: 10.1109/TPEL.2020.2969685.

[31] Z. Huang, S.-C. Wong, and C. K. Tse, "Design methodology of a series-series inductive power transfer system for electric vehicle battery charger application," in *Proc. IEEE Energy Convers. Congr. Exposit. (ECCE)*, Pittsburgh, PA, USA, Sep. 2014, pp. 1778–1782.

[32] C. Chen et al., "Modeling and decoupled control of inductive power transfer to implement constant current/voltage charging and ZVS operating for electric vehicles," *IEEE Access*, vol. 6, pp. 59917–59928, 2018.

[33] K. Colak, E. Asa, M. Bojarski, D. Czarkowski, and O. C. Onar, "A novel phase-shift control of semibridgeless active rectifier for wireless power transfer," *IEEE Trans. Power Electron.*, vol. 30, no. 11, pp. 6288–6297, Nov. 2015.

[34] D. Patil, M. Sirico, L. Gu, and B. Fahimi, "Maximum efficiency tracking in wireless power transfer for battery charger: Phase shift and frequency control," in *Proc. IEEE Energy Convers. Congr. Exposit. (ECCE)*, Milwaukee, WI, USA, Sep. 2016, pp. 1–8.

[35] Q. Chen, S. C. Wong, C. K. Tse, and X. Ruan, "Analysis, design, and control of a transcutaneous power regulator for artificial hearts," *IEEE Trans. Biomed. Circuits Syst.*, vol. 3, no. 1, pp. 23–31, Feb. 2009.

[36] A. Berger, M. Agostinelli, S. Vesti, J. A. Oliver, J. A. Cobos, and M. Huemer, "A wireless charging system applying phase-shift and amplitude control to maximize efficiency and extractable power," *IEEE Trans. Power Electron.*, vol. 30, no. 11, pp. 6338–6348, Nov. 2015.

[37] W. Zhang, S.-C. Wong, C. K. Tse, and Q. Chen, "Load-independent duality of current and voltage outputs of a series-or parallel-compensated inductive power transfer converter with optimized efficiency," *IEEE J. Emerg. Sel. Topics Power Electron.*, vol. 3, no. 1, pp. 137–146, Mar. 2015.

[38] W. Zhang, S.-C. Wong, C. K. Tse, and Q. Chen, "Analysis and comparison of secondary series-and parallel-compensated inductive power transfer systems operating for optimal efficiency and load-independent voltage-transfer ratio," *IEEE Trans. Power Electron.*, vol. 29, no. 6, pp. 2979–2990, Jun. 2014.

[39] C.-S. Wang, G. A. Covic, and O. H. Stielau, "Power transfer capability and bifurcation phenomena of loosely coupled inductive power transfer systems," *IEEE Trans. Ind. Electron.*, vol. 51, no. 1, pp. 148–157, Feb. 2004.

[40] S. Jayalath and A. Khan, "Analysis of the relationship between the parameters of IPT transformer and power electronic system," in *Proc. IEEE Wireless Power Transf. Conf. (WPTC)*, Jun. 2018, pp. 1–4.

[41] X. Qu, W. Zhang, S.-C. Wong, and C. K. Tse, "Design of a current-source-output inductive power transfer LED lighting system," *IEEE J. Emerg. Sel. Topics Power Electron.*, vol. 3, no. 1, pp. 306–314, Mar. 2015.

[42] K. Ogata. *Modern Control Engineering*, 5th ed. London, U.K.: Pearson, 2009.

[43] G. C. Goodwin, S. F. Graebe, and M. E. Salgado, *Control System Design*, vol. 240. Upper Saddle River, NJ, USA: Prentice-Hall, 2001.

[44] S. Buso and P. Mattavelli, *Digital Control in Power Electronics*. San Rafael, CA, USA: Morgan & Claypool, 2015.

[45] K. Aditya, S. S. Williamson, and V. K. Sood, "Impact of zero-voltage switching on efficiency and power transfer capability of a series-series compensated IPT system," in *Proc. IEEE Transp. Electrific. Conf. (ITEC-India)*, Pune, India, Dec. 2017, pp. 1–7.

Io-Wa Iam (Student Member, IEEE) received the B.Sc. degree in electrical and computer engineering from the University of Macau (UM), Macao, China, in 2020, where he is currently pursuing the Ph.D. degree in electrical and computer engineering.

In 2019, he was a Vice President of the UM Student Branch under IEEE Macau. His current research interests include power electronics and wireless power transfer.

Mr. Iam was awarded the "Best Track Paper Award" in APPEEC 2019.

Iok-U Hoi (Student Member, IEEE) received the B.Sc. degree in electrical and computer engineering from the University of Macau (UM), Macao, China, in 2020, where he is currently pursuing the M.Sc. degree in electrical and computer engineering.

In 2019, he was a Deputy Chief Financial Officer of the UM Student Branch under IEEE Macau. His current research interests include power electronics and wireless power transfer.

Mr. Hoi was awarded the "Best Track Paper Award" in APPEEC 2019.

Zhicong Huang (Member, IEEE) received the B.Eng. degree in electrical engineering and automation and the M.Phil. degree in mechanical and electronic engineering from the Huazhong University of Science and Technology, Wuhan, China, in 2010 and 2013, respectively, and the Ph.D. degree in power electronics from The Hong Kong Polytechnic University, Hong Kong, in 2018.

He is currently an Assistant Professor with the Shien-Ming Wu School of Intelligent Engineering, South China University of Technology, Guangzhou, China. In 2019, he was a Post-Doctoral Fellow under the UM Macao Talent Program with the State Key Laboratory of Analog and Mixed-Signal VLSI, University of Macau, Macao, China. His research interests include wireless power transfer, electric vehicles, and artificial intelligence.
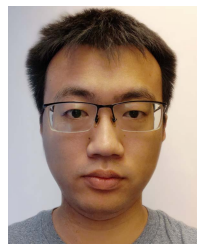
Cheng Gong (Graduate Student Member, IEEE) received the M.Sc. degree in electrical engineering from Guangxi University, Nanning, China, in 2017. He is currently pursuing the Ph.D. degree in electrical and computer engineering with the University of Macau (UM), Macau, China.

His research interests include power quality compensators, converter controller design, and power electronic-based power systems.

Chi-Seng Lam (Senior Member, IEEE) received the Ph.D. degree in electrical and electronics engineering from the University of Macau (UM), Macao, China, in 2012.

He completed the Clare Hall Study Program in the University of Cambridge, Cambridge, U.K., in 2019. From 2006 to 2009, he was an Electrical and Mechanical Engineer with UM. From 2009 to 2012, he simultaneously worked as a Laboratory Technician with UM and pursued his Ph.D. degree. In 2013, he was a Post-Doctoral Fellow with The Hong Kong Polytechnic University, Hong Kong. He is currently an Associate Professor with the State Key Laboratory of Analog and Mixed-Signal VLSI and the Institute of Microelectronics, UM, where he is also with the Department of Electrical and Computer Engineering, Faculty of Science and Technology. He has coauthored or co-edited four books and more than 100 technical journals and conference papers. He holds four U.S. and two Chinese patents. His research interests include power quality compensators, renewable energy generation, integrated power electronics controllers, power management integrated circuits, and wireless power transfer.

Dr. Lam was a recipient or co-recipient of the IEEE PES Chapter Outstanding Engineer Award in 2016, the Best Track Paper Award of APPEEC 2019, the Best Paper Award of ICTA 2019, the Merit Paper Award of the third RIUPEEEC Conference in 2005, the Macao Science and Technology Invention Award (Second Class and Third Class), and the Research and Development Award for Postgraduates (Ph.D.) in 2018, 2014, and 2012, respectively. He was the Vice-Chair of the IEEE Macau Section from 2016 to 2020 and the Chair of the IEEE Macau CAS Chapter from 2017 to 2018. He is currently the Chair of the IEEE Macau IES Chapter and the Power Quality Subcommittee Chair of the IEEE IES Technical Committee on Power Electronics. He serves as an Associate Editor for the IEEE ACCESS and a Guest Editor for the IEEE TRANSACTIONS ON CIRCUITS AND SYSTEMS II: EXPRESS BRIEFS and the *IET Power Electronics* in 2020. He served as a member of the Organizing Committee or the Technical Program Committee of several IEEE international conferences, including IECON 2019, ASSCC 2019, APPEEC 2019, IECON 2018, IESES 2018, ASP-DAC 2016, and TENCON 2015.

Pui-In Mak (Fellow, IEEE) received the Ph.D. degree from the University of Macau (UM), Macao, China, in 2006.

He is currently a Full Professor with the ECE Department, UM Faculty of Science and Technology, and the Associate Director (Research) at the UM Institute of Microelectronics and the State Key Laboratory of Analog and Mixed-Signal VLSI. His research interests are on analog and radio frequency (RF) circuits and systems for wireless and multidisciplinary innovations.

Dr. Mak has been a fellow of the U.K. Institution of Engineering and Technology (IET) for contributions to engineering research, education and services since 2018, the IEEE for contributions to radio frequency and analog circuits since 2019, and the U.K. Royal Society of Chemistry since 2020. He (co)-received the DAC/ISSCC Student Paper Award in 2005, the CASS Outstanding Young Author Award in 2010, the National Scientific and Technological Progress Award in 2011, the Best Associate Editor of the IEEE TRANSACTIONS ON CIRCUITS AND SYSTEMS II: EXPRESS BRIEFS in 2012–2013, the A-SSCC Distinguished Design Award in 2015, and the ISSCC Silkroad Award in 2016. In 2005, he was decorated with the Honorary Title of Value for scientific merits by the Macau Government. He is/was the TPC Vice Co-Chair of ASP-DAC in 2016 and a TPC Member of A-SSCC from 2013 to 2016 and in 2019, ESSCIRC from 2016 to 2017, and ISSCC from 2017 to 2019. He was the Chairman of the Distinguished Lecturer Program of the IEEE Circuits and Systems Society from 2018 to 2019. His involvements with IEEE are an Editorial Board Member of the IEEE Press from 2014 to 2016, a member of the Board-of-Governors of the IEEE Circuits and Systems Society from 2009 to 2011, a Senior Editor of the IEEE JOURNAL ON EMERGING AND SELECTED TOPICS IN CIRCUITS AND SYSTEMS from 2014 to 2015, and an Associate Editor of the IEEE JOURNAL OF SOLID-STATE CIRCUITS since 2018, the IEEE SOLID-STATE CIRCUITS LETTERS since 2017, the IEEE TRANSACTIONS ON CIRCUITS AND SYSTEMS I: REGULAR PAPERS from 2010 to 2011 and from 2014 to 2015, and the IEEE TRANSACTIONS ON CIRCUITS AND SYSTEMS II: EXPRESS BRIEFS from 2010 to 2013. He is/was a Distinguished Lecturer of the IEEE Circuits and Systems Society from 2014 to 2015 and the IEEE Solid-State Circuits Society from 2017 to 2018. He has been inducted as an Overseas Expert of the Chinese Academy of Sciences since 2018.

Rui Paulo Da Silva Martins (Fellow, IEEE) was born in April 30, 1957. He received the bachelor's, master's, and Ph.D. degrees, as well as the Habilitation for Full Professor in electrical engineering and computers from the Department of Electrical and Computer Engineering (DECE), Instituto Superior Técnico (IST), University of Lisbon, Lisbon, Portugal, in 1980, 1985, 1992, and 2001, respectively.

He has been with DECE/IST, University of Lisbon, since October 1980. Since 1992, has been on leave from the University of Lisbon and with DECE, Faculty of Science and Technology (FST), University of Macau (UM), Macao, China, where he has been a Chair Professor since August 2013. He was the Dean of FST from 1994 to 1997, and has been a Vice-Rector of UM since 1997. From September 2008 to August 2018, he was a Vice-Rector of Research and from September 2018 to August 2023, a Vice-Rector of Global Affairs. Within the scope of his teaching and research activities, he has taught 21 bachelor's and master's courses and, in UM, he has supervised (or cosupervised) 47 theses: Ph.D. (26) and master's (21). He has coauthored 7 books and 12 book chapters; 537 articles, in scientific journals (217) and in conference proceedings (320); holds 36 Patents: USA (32), Taiwan (3), and China (1); as well as other 64 academic works, in a total of 656 publications. He created in 2003 the Analog and Mixed-Signal VLSI Research Laboratory of UM elevated in January 2011 to the State Key Laboratory (SKLAB) of China (the First in Engineering in Macao), being its Founding Director. He was the Founding Chair of UMTEC (UM company) from January 2009 to March 2019, supporting the incubation and creation of Digifluidic in 2018, the first UM spin-off, whose CEO is an SKLAB Ph.D. graduate. He was also a Co-Founder of Chipidea Microelectronics (Macao) [now Synopsys-Macao] in 2001/2002.

Prof. Rui Martins was the Founding Chair of the IEEE Macau Section from 2003 to 2005 and the IEEE Macau Joint-Chapter on Circuits and Systems (CAS)/Communications (COM) from 2005 to 2008 [2009 World Chapter of the Year of the IEEE CAS Society (CASS)], the General Chair of the IEEE Asia–Pacific Conference on CAS—APCCAS'2008, the Vice-President (VP) of Region 10 (Asia, Australia, and Pacific) from 2009 to 2011, the VP of the World Regional Activities and Membership of the IEEE CASS from 2012 to 2013, an Associate Editor of the IEEE TRANSACTIONS ON CAS II: EXPRESS BRIEFS from 2010 to 2013, and nominated as the Best Associate Editor from 2012 to 2013. He was also a member of the IEEE CASS Fellow Evaluation Committee in 2013, 2014, and 2018 and the Chair in 2019 and 2021; the IEEE Nominating Committee of Division I Director (CASS/EDS/SSCS) in 2014; and the IEEE CASS Nominations Committee from 2016 to 2017. Plus, he was the General Chair of the ACM/IEEE Asia South Pacific Design Automation Conference—ASP-DAC'2016, receiving the IEEE Council on Electronic Design Automation (CEDA) Outstanding Service Award in 2016, and also the General Chair of the IEEE Asian Solid-State Circuits Conference—A-SSCC 2019. He was also the Vice-President (2005–2014) and the President (2014–2017) of the Association of Portuguese Speaking Universities (AULP), and received two Macao Government decorations: the Medal of Professional Merit (Portuguese-1999) and the Honorary Title of Value (Chinese-2001). In July 2010, he was elected, unanimously, as a Corresponding Member of the Lisbon Academy of Sciences, being the only Portuguese Academician living in Asia.